Chinese Chemical Letters 35 (2024) 108583

Contents lists available at ScienceDirect

Chinese Chemical Letters

journal homepage: www.elsevier.com/locate/cclet

Low-temperature selective synthesis of metastable α-MoC with electrochemical properties: Electrochemical co-reduction of CO_2 and MoO_3 in molten salts

Longtao Zhu[a], Yinan Zhao[a], Wenhao Yang[a], Hsien-Yi Hsu[b], Ping Peng[a,*], Fang-Fang Li[a,*]

[a] School of Materials Science and Engineering, Huazhong University of Science and Technology, Wuhan 430074, China
[b] School of Energy and Environment & Department of Materials Science and Engineering, City University of Hong Kong, Hong Kong 999077, China

ARTICLE INFO

Article history:
Received 26 March 2023
Revised 13 May 2023
Accepted 16 May 2023
Available online 20 May 2023

Keywords:
α-MoC
CO_2 electroreduction
Molten salt
Sulfur doping
Hydrogen evolution reaction

ABSTRACT

Metastable molybdenum carbide (α-MoC), as a catalyst and an excellent support for metal catalysts, has been widely used in thermo/electro-catalytic reactions. However, the selective synthesis of α-MoC remains a great challenge. Herein, a simple one-pot synthetic strategy for the selective preparation of metastable α-MoC is proposed by electrochemical co-reduction of CO_2 and MoO_3 in a low-temperature eutectic molten carbonate. The synthesized α-MoC shows a reed flower-like morphology. By controlling the electrolysis time and monitoring the phase and morphology of the obtained products, the growth process of α-MoC is revealed, where the carbon matrix is deposited first followed by the growth of α-MoC from the carbon matrix. Moreover, by analyzing the composition of the electrolytic products, the formation mechanism for α-MoC is proposed. In addition, through this one-pot synthetic strategy, S-doped α-MoC is successfully synthesized. Density functional theory (DFT) calculations reveal that S doping enhanced the HER performance of α-MoC by facilitating water absorption and dissociation and weakening the bond energy of Mo-H to accelerate H desorption. The present work not only highlights the valuable utilization of CO_2 but also offers a new perspective on the design and controllable synthesis of metal carbides and their derivatives.

Transition metal carbides (TMCs), owing to their high electrical conductivity, excellent durability as well as wide pH applicability, have attracted great attention in the materials science community [1–4]. Among them, molybdenum carbides possess similar d-band electronic structures to platinum [5,6], which makes them widely used in catalytic reactions such as ammonia preparation and decomposition [7–9], steam reforming of methanol [10,11], water-gas shift (WGS) reaction [12–14], and electrochemical hydrogen evolution reaction (HER) [15–19]. Besides, molybdenum carbides can also be used for energy storage [20,21]. The hexagonal-close-packed β-Mo_2C and the metastable face-centered-cubic α-MoC are the most studied molybdenum carbide phases. Compared with β-Mo_2C, α-MoC has a d-band center closer to the Fermi level, which is favorable for the adsorption and dissociation of water molecules, thus, α-MoC-based catalysts exhibited higher activity than β-Mo_2C-based catalysts in methanol steam reforming, WGS reaction, and alkaline HER [11,12,22]. In addition, α-MoC exhibits stronger interactions with metals than β-Mo_2C, so it has been used as a support for metal species with catalytic activity. A series of high-performance M/α-MoC (M = Pt, Ru, Ir, Au, and Ni) heterogeneous catalysts have been established. Due to the strong metal-support interaction, α-MoC not only facilitated the stabilization of metal single atoms and/or metal clusters but also promoted the catalytic activity of the metal centers *via* optimizing adsorption/desorption of the reactants and intermediates on the catalysts surface [10–13,17,23,24].

Nevertheless, compared with the thermally stable β-Mo_2C phase, the selective synthesis of the pure metastable α-MoC phase remains challenging because of the complex procedures, noble metal requirement, and high energy input [22,25–27]. The current synthesis method for α-MoC mainly relies on the high-temperature carbonization/carburization of Mo-containing precursors, which often cause the aggregation and coked surfaces of α-MoC to prevent the exposure of active sites [17,28–31]. Moreover, the usage of combustible/explosive gas reductant, *i.e.* CH_4/H_2 for α-MoC is highly dangerous [26,27,32–34]. In addition, the carbon sources for the preparation of α-MoC are usually environment-unfriendly organic compounds [23,24,35]. Thus, given

* Corresponding authors.
E-mail addresses: ppeng@hust.edu.cn (P. Peng), ffli@hust.edu.cn (F.-F. Li).

https://doi.org/10.1016/j.cclet.2023.108583
1001-8417/

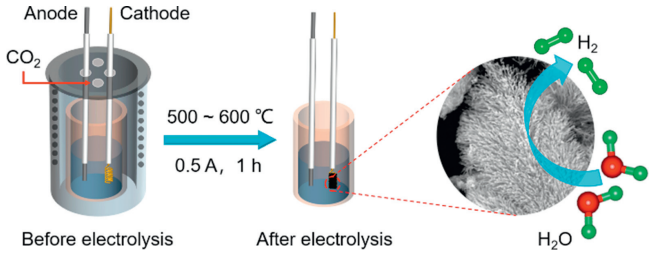

Scheme 1. Schematic illustration for the synthesis of α-MoC or S-doped α-MoC in molten salts.

the highly valuable applications of α-MoC and the present harsh synthetic conditions, a simple low-temperature process to selectively synthesize the α-MoC phase is urgently needed.

Carbon dioxide (CO_2) is a predominant greenhouse gas but is also an abundant and cost-effective carbon feedstock for producing high-value carbon materials. In molten salt media, CO_2 can be efficiently captured [36,37] and electrochemically converted into highly valuable nanocarbons [38–44] and metal-carbon composites [45–48]. Molten salts bear low toxicity, low cost, and high ionic conductivity. Moreover, molten media has wide electrochemical and temperature windows (200-1000 °C), which can be tuned by changing the composition of the molten salts as well as the proportion of the salts. Therefore, using CO_2 as the carbon source for the selective synthesis of α-MoC in the low-temperature molten salt is a low-cost sustainable approach, which is expected to address the aforementioned issues associated with the low-selectivity and harsh synthesis conditions. In addition, the growth process and formation mechanism of α-MoC in molten media are rarely studied. Understanding the reaction process and kinetics is important for the design and synthesis of α-MoC-based/supported materials.

In this work, we propose a simple method for selective synthesis of metastable α-MoC phase by electrochemical co-reduction of CO_2 and MoO_3 in molten carbonates at low temperatures (500-600 °C). The as-synthesized α-MoC shows a reed flower-like morphology composed of ultrafine MoC particles. The growth process for α-MoC was revealed by controlling the electrolysis time and monitoring the as-obtained samples by *ex-situ* XRD and TEM. The formation mechanism was unraveled by analyzing the composition of the electrolytic products. In addition, by introducing Li_2SO_4 into the molten carbonate electrolyte, S-doped α-MoC was synthesized in one step. S-doped α-MoC exhibits enhanced alkaline HER activity relative to α-MoC, which was rationalized by density functional calculations (DFT). The present work not only provides a new perspective for understanding the formation of α-MoC but also offers an alternative approach to the synthesis of metal carbides and their derivatives.

As illustrated in Scheme 1, the eutectic carbonate (Li_2CO_3, Na_2CO_3, and K_2CO_3) and molybdenum source (MoO_3) are melted at different temperatures (500 °C, 550 °C, and 600 °C) to serve as the electrolyte. A graphite rod and a galvanized steel with a spring-like shape are used as the anode and the cathode (see photographs of the cathode before and after electrolysis in Fig. S1 (Supporting information), respectively. After a constant current of 0.5 A is applied for 1 h, α-MoC is deposited on the surface of the cathode. The corresponding electrolysis curves are shown in Fig. S2 (Supporting information). The electrolytic products are washed with acid and deionized water to obtain the α-MoC products. α-MoC obtained at different temperatures are named α-MoC-500, α-MoC-550, and α-MoC-600, respectively.

The structures of the synthesized samples were first characterized by X-ray diffraction (XRD). As shown in Fig. 1a, four peaks located at 36.4°, 42.3°, 61.4°, and 73.5°, respectively correspond to the (111), (200), (220), and (311) planes of α-MoC (PDF# 89-2868) [28], indicating the successful synthesis of α-MoC. To analyze the surface chemical constituent of the samples, X-ray photoelectron spectroscopy (XPS) was performed. The survey spectra (Fig. S3 in Supporting information) show that α-MoC obtained at different temperatures consists of C, Mo, and O elements. The high-resolution XPS spectra of Mo 3d can be deconvoluted into eight peaks (Fig. 1b and Table S1 in Supporting information), which represent the four valence states (+2, +3, +4, and +6) of the Mo element. The peaks of Mo^{2+} and Mo^{3+} are associated with the Mo-C bond, and the peaks of Mo^{4+} and Mo^{6+} correspond to MoO_2 and MoO_3 due to the surface oxidation of the samples in the air [47,48], which accounts for the presence of O element in the full XPS survey (Fig. S3). Besides, the C 1s spectra of α-MoC were also analyzed, and there are four peaks in the C 1s spectrum, representing the C-Mo, C-C, C-O, and C=O bonds (Fig. 1c and Table S2 in Supporting information) [49,50].

The morphology of the samples was examined by scanning electron microscopy (SEM). α-MoC prepared at different temperatures showed a reed flower-like morphology (Figs. 1d–f). TEM analysis of the representative α-MoC-550 indicated that each branch of reed flowers consists of many small particles with a size distribution of 1.91 ± 0.34 nm (Fig. 1g). The lattice fringes of the particles have an interplanar spacing of 0.246 nm, corresponding to the (111) plane of α-MoC (Fig. 1h), which indicates that α-MoC particles are well crystallized at 550 °C. Moreover, a uniform distribution of α-MoC nanoparticles was observed from the HAADF-STEM and the corresponding EDS elemental mapping images of α-MoC-550 (Figs. 1i–l). As the electrolysis temperature increases to 600 °C, α-MoC-600 presents larger grains with a size of 2.23 ± 0.27 nm (Figs. S4a and b in Supporting information). Whereas, α-MoC-500 obtained at a low temperature of 500 °C mainly shows an amorphous structure with only crystallization in local areas (Figs. S4c and d in Supporting information).

In order to study the growth process of α-MoC, we conducted control experiments by controlling the electrolysis time and monitored the reaction by *ex-situ* XRD and TEM. The electrolysis was carried out at 550 °C $Li_2CO_3/Na_2CO_3/K_2CO_3$ electrolyte for 5 min, 10 min, 15 min, and 20 min, and the corresponding products are named α-MoC-550-5, α-MoC-550-10, α-MoC-550-15, and α-MoC-550-20, respectively. XRD patterns for the products were plotted in Fig. 2a. When the electrolysis time is controlled at 5 min, the XRD pattern of α-MoC-550-5 is mainly the diffraction peaks of carbon. With the extension of electrolytic time from 5 min to 10 min, 15 min, and 20 min, the carbon peaks gradually decreased and the characteristic peaks of α-MoC are correspondingly enhanced, indicating the gradual conversion of carbon into MoC.

SEM images of the products obtained at different times are shown in Figs. 2b–e. The carbon obtained by 5 min electrolysis is amorphous (Fig. 2b), and then some spherical particles start to grow out from the carbon matrix (Fig. 2c). Interestingly, when the electrolysis time was extended to 15 min, some branches start to grow out from the surface of spherical particles (Fig. 2d). At 20 min, α-MoC with reed-flower like morphology was formed (Fig. 2e). To identify the structure of the spherical particles in Fig. 2c, TEM analysis was performed, which showed that the spherical particles attached to the carbon substrate (Fig. 2f). HR-TEM and the corresponding selected-area electron diffraction pattern (SAED) revealed that the spherical particle is composed of smaller α-MoC crystalline grains with a lattice space of 0.246 nm, corresponding to the (111) plane of α-MoC (Figs. 2g–i). The diffraction rings from inside to outside represent the (111), (200), (220), and (311) planes of α-MoC, respectively (Fig. 2i). Based on the above analysis, we proposed the formation process of α-MoC as follows: The carbon substrate was first deposited on the cathode surface, and then the

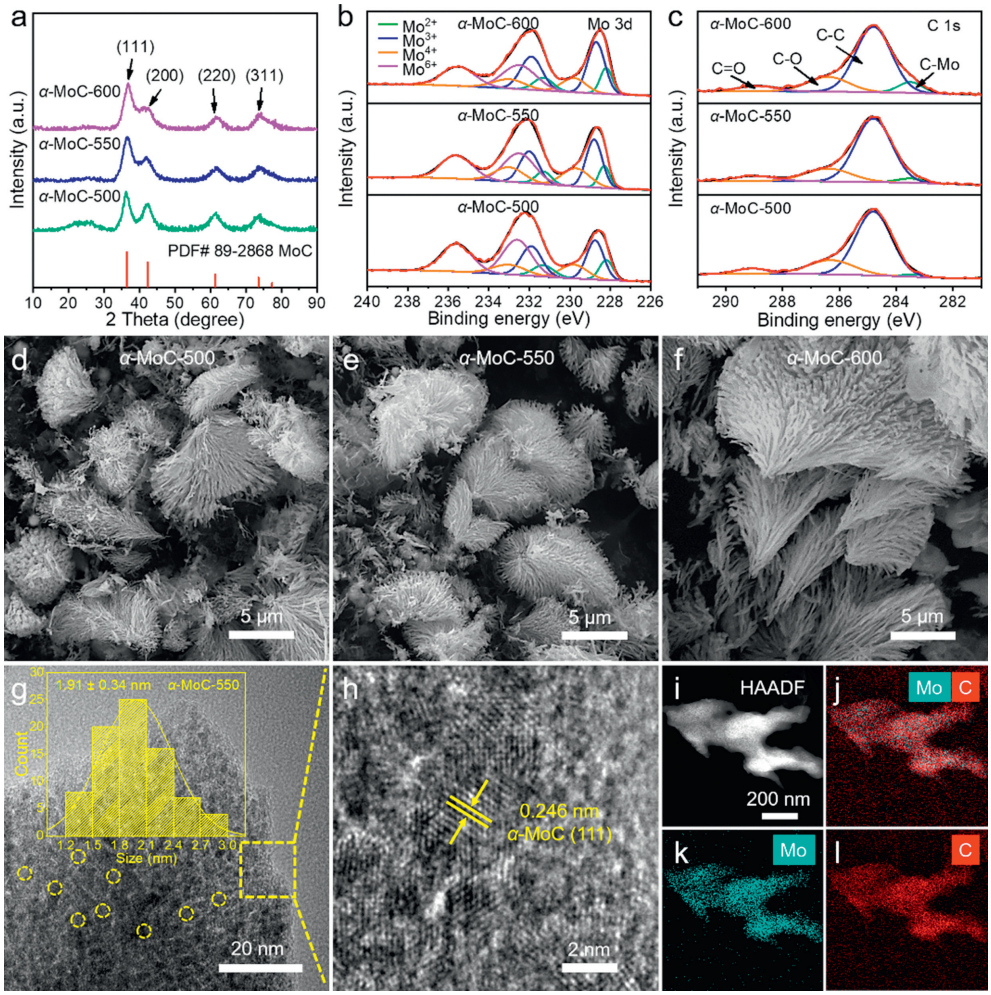

Fig. 1. (a) XRD patterns, (b, c) the high-resolution XPS spectra of Mo 3d and C 1s, (d–f) SEM images of the synthesized α-MoC at different temperatures. (g, h) HR-TEM images, (i–l) HAADF-STEM and the corresponding EDS elemental mapping images of α-MoC-550.

spherical α-MoC grains are grown out from the carbon substrate and served as the nucleation sites for α-MoC growth.

To unravel the formation mechanism of α-MoC, we analyzed the composition of the electrolytic products which were treated with different washing conditions. The cathodic product without washing presents a color grey (Fig. S5 in Supporting information) and an irregular morphology (Fig. S6a in Supporting information) since the electrolyte is wrapped around the product. The XRD pattern of the unwashed product showed the characteristic diffraction of $LiNaCO_3$ and $(Li_{0.5}K_{0.5})_2CO_3$ (Fig. 2j) due to the formation of new carbonates by melting, cooling, and recrystallization of Li_2CO_3, Na_2CO_3, and K_2CO_3. Notably, the diffraction peaks of $K_3Na(MoO_4)_2$ were also observed in the XRD spectrum and $K_3Na(MoO_4)_2$ served as the Mo source for the formation of α-MoC. Unfortunately, due to the strong diffraction peaks of the electrolyte, the signals of α-MoC were masked. When the electrolytic product was washed with deionized water, the sample appeared black (Fig. S5), indicating that most of the carbonate electrolytes were eluted, but its morphology remained heterogeneous (Fig. S6b in Supporting information). Consistent results were obtained from its XRD analysis. The diffraction peaks of $LiNaCO_3$, $(Li_{0.5}K_{0.5})_2CO_3$, and $K_3Na(MoO_4)_2$ disappeared and the diffraction peaks of α-MoC and Li_2MoO_3 were observed in this water-washed product (Fig. 2k). The appearance of Li_2MoO_3 is owing to the cathodic reduction of MoO_4^{2-} to MoO_3^{2-}, which combines with Li^+ in the electrolyte to form the water-insoluble Li_2MoO_3. Further, when the electrolytic product is treated with acid, the product showed black color (Fig. S5) and a homogeneous reed-flower morphology (Fig. S6c in Supporting information), indicating that the carbonate electrolyte was completely removed. Consistent results were obtained from the XRD spectrum, in which only the diffraction peaks of α-MoC were presented (Fig. 2l).

Notably, $K_3Na(MoO_4)_2$ was detected in the electrolytic product (Fig. 2j). To understand the formation of MoO_4^{2-}, tail gases evolved from MoO_3-mixed Li/Na/K carbonates (without electrolysis) at room temperature and 550 °C (without electrolysis) were analyzed under Ar gas flow. As displayed in Figs. S7a and b (Supporting information), the volume of O_2 collected at room temperature (0.44%) and 550 °C (0.48%) was almost the same. As the temperature increased from room temperature to 550 °C, the CO_2 content sharply increased from 0.27% to 13.02%, which indicated that the MoO_4^{2-} came from the spontaneous reaction between MoO_3 and carbonate ($MoO_3 + CO_3^{2-} \rightarrow MoO_4^{2-} + CO_2$) at 550 °C. Furthermore, the composition of tail gases before and after the electrolysis under CO_2 atmosphere at 550 °C was analyzed (Figs. S7c and d in Supporting information). The O_2 content increased from 0.72% to 2.42%, and the CO_2 content decreased from 90.83% to 87.14%, suggesting the capture and conversion of CO_2 as well as the formation of O_2 during the electrolysis process.

Based on the above results, the formation mechanism of α-MoC by molten salt electrolysis can be proposed as follows: MoO_3 reacted with CO_3^{2-} to form MoO_4^{2-} and CO_2 (Eq. 1). CO_2 was

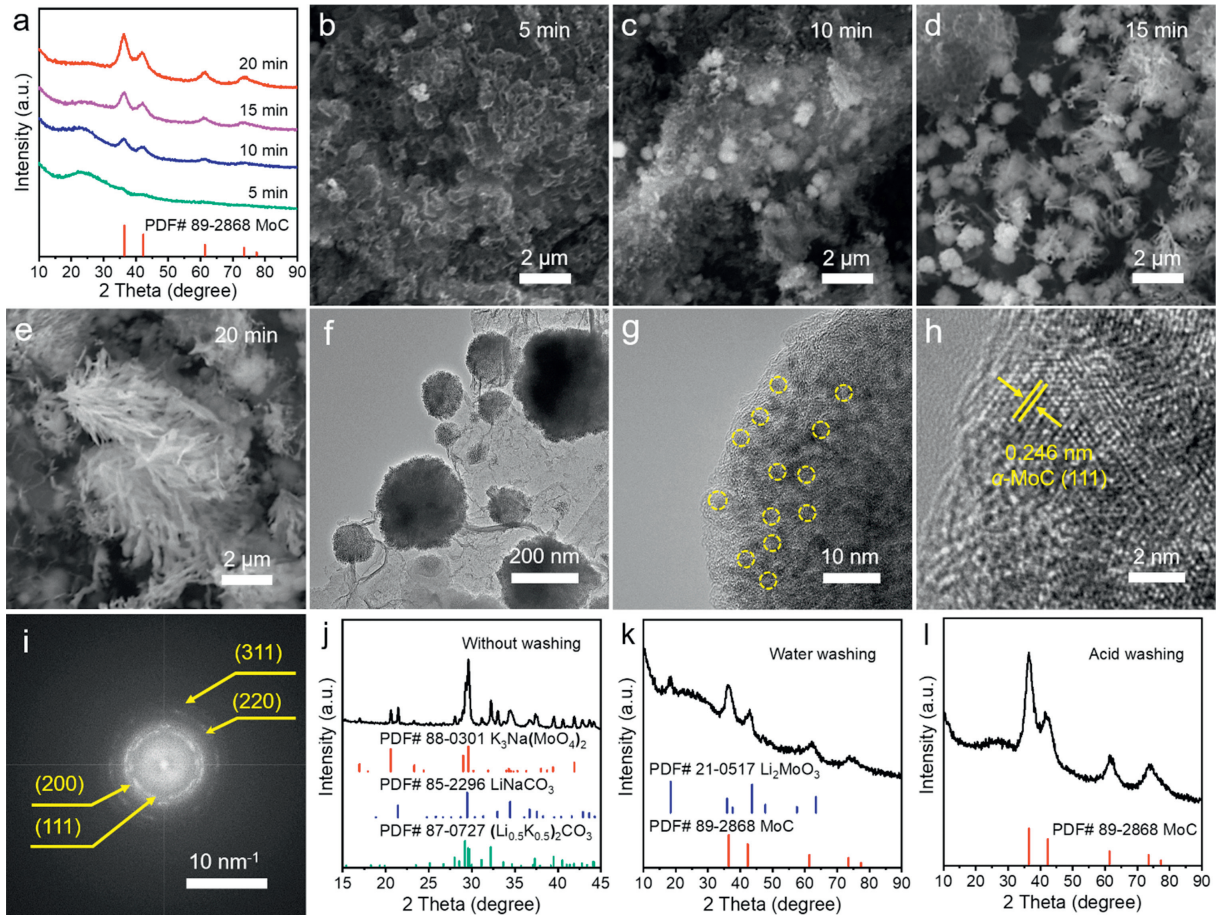

Fig. 2. (a) XRD patterns of the samples obtained at electrolysis times of 5 min, 10 min, 15 min, and 20 min, respectively. (b–e) SEM images of α-MoC-550-5, α-MoC-550-10, α-MoC-550-15, and α-MoC-550-20. (f) TEM image of α-MoC-550-10. (g, h) HR-TEM images and (i) the corresponding selected-area electron diffraction pattern (SAED) of α-MoC-550-10. XRD patterns of the electrolytic products (j) without washing, (k) with water washing, and (l) with acid washing.

captured by O^{2-} generated from the electroreduction of MoO_4^{2-} (Eq. 2) and/or CO_3^{2-} splitting (Eq. 3) to regenerate the CO_3^{2-} (Eq. 4). The electroreduction of MoO_4^{2-} also produced the MoO_3^{2-} (Eq. 2), which was co-reduced with C generated from CO_3^{2-} reduction (Eq. 3) to form α-MoC (Eq. 5). The generated O^{2-} ions (Eqs. 2 and 3) played two roles in this conversion process. Part of O^{2-} was oxidized to O_2 by losing electrons at the anode (Eq. 6), and the rest of O^{2-} captured CO_2 to regenerate CO_3^{2-} (Eq. 4) [36,37]. Thus, the net reaction is the co-reduction of MoO_3 and CO_2 to form the α-MoC and release the O_2 (Eq. 7). The detailed reaction process can be found in Fig. S8 (Supporting information). The electrolytic efficiency for α-MoC synthesized at 500, 550, and 600 °C is 63.18%, 66.40%, and 72.56%, respectively (Table S3 in Supporting information).

$$MoO_3 + CO_3^{2-} \rightarrow MoO_4^{2-} + CO_2 \quad (1)$$

$$MoO_4^{2-} + 2e^- \rightarrow MoO_3^{2-} + O^{2-} \quad (2)$$

$$CO_3^{2-} + 4e^- \rightarrow C + 3O^{2-} \quad (3)$$

$$2CO_2 + 2O^{2-} \rightarrow 2CO_3^{2-} \quad (4)$$

$$MoO_3^{2-} + 4e^- + C \rightarrow MoC + 3O^{2-} \quad (5)$$

$$5O^{2-} - 10e^- \rightarrow 5/2O_2 \quad (6)$$

$$2MoO_3 + 2CO_2 \rightarrow 2MoC + 5O_2 \quad (7)$$

In addition, we also performed the electrolysis in $Li_2CO_3/Na_2CO_3/K_2CO_3$ electrolyte without adding MoO_3, where a Mo anode was used instead of a graphite rod anode (Fig. S9 in Supporting information). As expected, the XRD pattern of the electrolytic product is consistent with that of α-MoC (Fig. S10 in Supporting information). The SEM images of the obtained product also show a reed flower-like morphology (Fig. S11 in Supporting information), indicating the formation of α-MoC. These results suggested that during the electrolysis, the Mo anode was *in-situ* oxidized to MoO_3 and served as the Mo source. Thus, α-MoC can be synthesized from CO_2 and *in-situ* generated MoO_3 in one step.

Molybdenum carbides have been applied as electrocatalysts in hydrogen evolution reactions (HER), and heteroatom doping is considered to be effective to promote catalytic performance [28,51,52]. Therefore, based on the preparation method of α-MoC, we also synthesized heteroatom-doped α-MoC. By adding Li_2SO_4 into the 550 °C molten $Li_2CO_3/Na_2CO_3/K_2CO_3$, S-doped α-MoC-550 was successfully obtained by one-step electrolysis. The XRD pattern (Fig. 3a), SEM (Fig. 3b), and TEM images (Fig. 3c) showed that the structure and morphology of S-doped α-MoC-550 are similar to that of α-MoC-550. Namely, S-doped α-MoC-550 shared the same reed flower-like morphology as α-MoC-550. S-doped α-MoC-550 is also composed of small crystalline α-MoC particles with a size

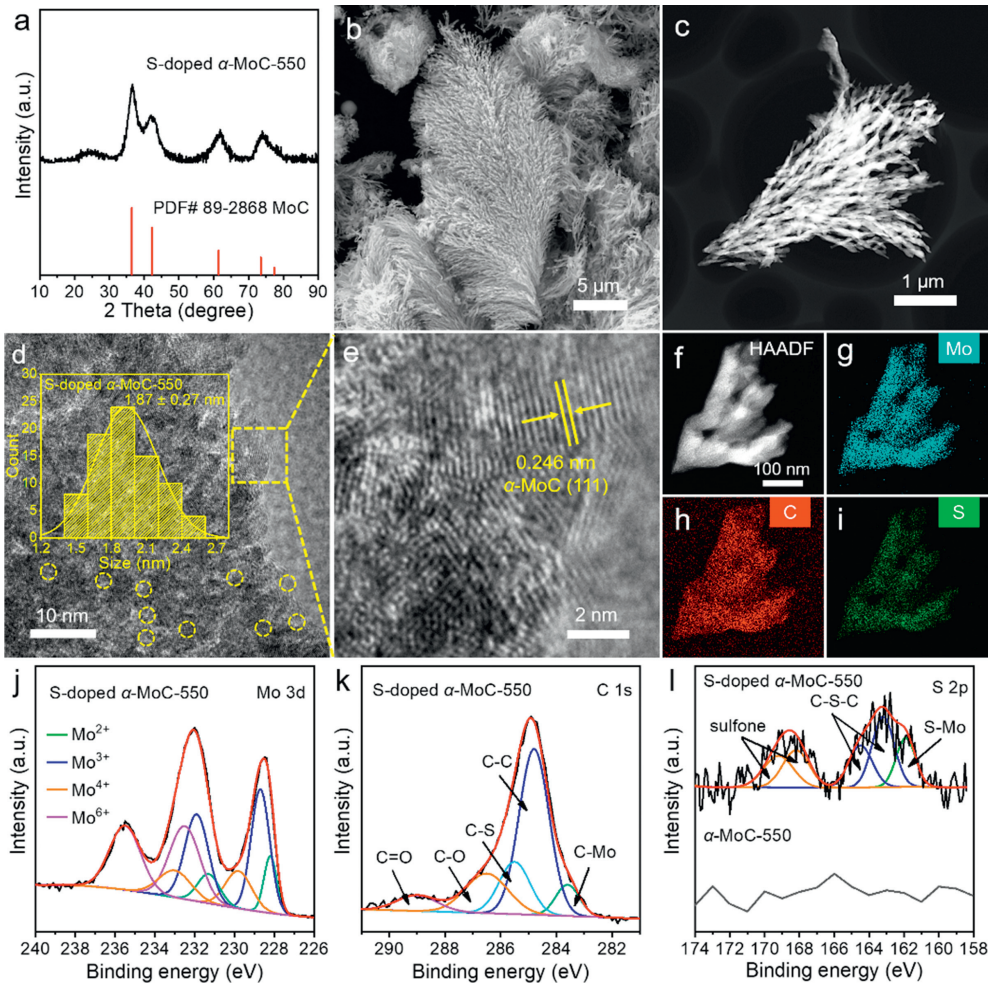

Fig. 3. (a) XRD pattern, (b) SEM, (c) HAADF-STEM, and (d, e) HR-TEM images of the synthesized S-doped α-MoC-550. (f–i) HAADF-STEM and the corresponding EDS elemental mapping images of S-doped α-MoC-550. The high-resolution XPS spectra of (j) Mo 3d, (k) C 1s, and (l) S 2p for S-doped α-MoC-550.

distribution of 1.87 ± 0.27 nm (Figs. 3d and e). The successful doping and uniform distribution of S element in S-doped α-MoC-550 was confirmed by its HAADF-STEM and the corresponding EDS elemental mapping (Figs. 3f–i). Element contents of S-doped α-MoC-550 according to EDS spectra were listed in Table S4 (Supporting information), where the content of S is *ca.* 3.49 wt%. The Mo 3d spectrum (Fig. 3j and Table S5 in Supporting information) of S-doped α-MoC-550 was also similar to that of α-MoC-550 (Fig. 1b). The C 1s spectrum (Fig. 3k and Table S6 in Supporting information) of S-doped α-MoC-550 can be split into five peaks, and the peak at 285.5 eV represents the C-S bond [53]. The S 2p spectrum (Fig. 3l and Table S7 in Supporting information) could be deconvoluted into five peaks, and the peak at 161.9 eV is associated with the S-Mo bond [54]. The peaks located at 163.2 eV and 164.5 eV were assigned to the C-S-C bond, and another two peaks at 168.2 eV and 169.2 eV were ascribed to the presence of sulfone [55,56]. The presence of the C-S bond (Fig. 3k) and the S-Mo bond (Fig. 3l) further elucidated the successful doping of S into α-MoC.

To assess the electrocatalytic performance of α-MoC and S-doped α-MoC toward HER, linear sweep voltammetry (LSV) was performed in 1 mol/L KOH (Fig. 4a). S-doped α-MoC performed better than α-MoC-550 for HER by showing a lower overpotential relative to α-MoC-550 at the same current density, which demonstrated the positive effect of S-doping on HER. Moreover, S-doped α-MoC-550 and α-MoC-550 show lower overpotentials than Pt/C at current densities larger than 133 and 149 mA/cm^2, respectively. The kinetics of HER was evaluated by calculating the Tafel slope (Fig. 4b), where the Tafel slope of S-doped α-MoC-550 is 80.2 mV/dec, smaller than that of α-MoC-550 (83.6 mV/dec), indicative of the fast HER kinetics of S-doped α-MoC-550 and a Volmer-Heyrovsky process [57]. The transport kinetics of electrodes was studied by electrochemical impedance spectroscopy (EIS). The Nyquist plot of S-doped α-MoC-550 shows a smaller semicircle than α-MoC-550 (Fig. 4c), representing a fast electron transfer process in the 1 mol/L KOH electrolyte. Additionally, the time-dependent current density curve of S-doped α-MoC-550 showed an ignored decline after the 10 h test compared with α-MoC-550 and Pt/C (Fig. 4d), indicating that S-doped α-MoC-550 has excellent stability. The enhanced activity of S-doped α-MoC-550 was rationalized by density functional theory (DFT) calculations. The models of MoC (111) and S-MoC (111) (Fig. S12 in Supporting information) were constructed based on the TEM and XPS results (Figs. 1h, 3e and l). Compared with MoC (111), S-MoC (111) has higher absorption energy and lower dissociation energy for water molecules (Fig. 4e) as well as an H absorption energy closer to zero (Fig. 4f), which is beneficial to water absorption, dissociation, and H desorption [58]. In addition, compared with MoC (111), the charge density around the Mo atom of S-MoC (111) is significantly reduced (Fig. S13 in Supporting information), which is attributed to the higher electronegativity of the S atom relative to

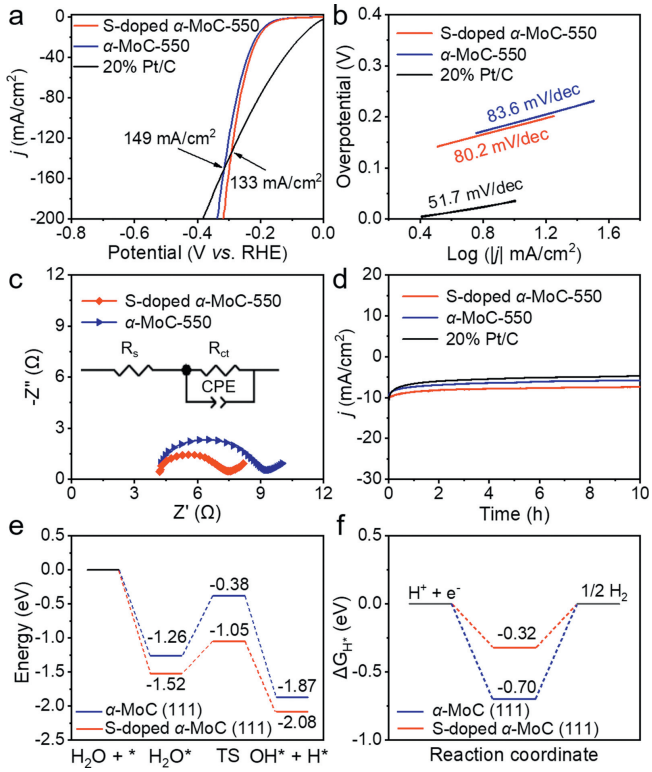

Fig. 4. (a) Polarization curves at a scan rate of 5 mV/s with a 90% iR-compensation in 1 mol/L KOH. (b) Tafel slopes. (c) Nyquist plots at the overpotential of 150 mV. The inset is an electrical equivalent circuit model. (d) The time-dependent current density curve. (e) Adsorption and dissociation energy of the H_2O molecule on the surface of α-MoC (111) and S-doped α-MoC (111). (f) Gibbs free energy diagrams of H adsorption on α-MoC (111) and S-doped α-MoC (111).

the Mo atom, leading to the charge transfer from Mo to S, thus weakening the bond energy of Mo-H [29] and facilitating the recombination of reactive hydrogen intermediates to produce H_2.

In summary, a low-temperature synthesis method for α-MoC was presented, in which CO_2 and MoO_3 were electrochemically co-reduced in 500-600 °C molten carbonates. The growth process of α-MoC suggested that the carbon substrate formed first followed by the growth of α-MoC. The *in-situ* formation of MoO_4^{2-} and the coupling reduction with CO_2 account for the formation of α-MoC. Understanding the growth of α-MoC will guide the design and synthesis of α-MoC-based materials. In addition, based on the preparation method for α-MoC, S-doped α-MoC was synthesized in one step by simply introducing Li_2SO_4 into the electrolyte. The S doping enhanced the HER performance of α-MoC by facilitating water absorption and dissociation and weakening the bond energy of Mo-H. This work not only demonstrated a facile way to prepare undoped/doped α-MoC but also provided in-depth insight into the formation mechanism of α-MoC. We propose that the strategy presented here could serve as a sustainable platform for the synthesis of other metal carbide materials.

Declaration of competing interest

The authors declare that they have no known competing financial interests or personal relationships that could have appeared to influence the work reported in this paper.

Acknowledgment

We appreciate the financial support from National Natural Science Foundation of China (Nos. 22071070, 21971077).

Supplementary materials

Supplementary material associated with this article can be found, in the online version, at doi:10.1016/j.cclet.2023.108583.

References

[1] Z. Chen, W. Gong, S. Cong, et al., Nano Energy 68 (2020) 104335.
[2] H. Jin, C. Guo, X. Liu, et al., Chem. Rev. 118 (2018) 6337–6408.
[3] Y. Ma, G. Guana, X. Hao, et al., Renew. Sustain. Energy Rev. 75 (2017) 1101–1129.
[4] H. Fan, H. Yu, Y. Zhang, et al., Angew. Chem. Int. Ed. 56 (2017) 12566–12570.
[5] D. Tian, S.R. Denny, K. Li, et al., Chem. Soc. Rev. 50 (2021) 12338–12376.
[6] J.R. Kitchin, J.K. Nørskov, M.A. Barteau, et al., Catal. Today 105 (2005) 66–73.
[7] Y. Wan, M. Zheng, R. Lv, Mater. Today Energy 32 (2023) 101240.
[8] H. Cheng, L.X. Ding, G.F. Chen, et al., Adv. Mater. 30 (2018) 1803694.
[9] W. Zheng, T.P. Cotter, P. Kaghazchi, et al., J. Am. Chem. Soc. 135 (2013) 3458–3464.
[10] L. Lin, Q. Yu, M. Peng, et al., J. Am. Chem. Soc. 143 (2021) 309–317.
[11] L. Lin, W. Zhou, R. Gao, et al., Nature 544 (2017) 80–83.
[12] X. Zhang, M. Zhang, Y. Deng, et al., Nature 589 (2021) 396–401.
[13] L. Sun, J. Xu, X. Liu, et al., ACS Catal. 11 (2021) 5942–5950.
[14] S. Yao, X. Zhang, W. Zhou, et al., Science 357 (2017) 389–393.
[15] X.F. Lu, L. Yu, J. Zhang, et al., Adv. Mater. 31 (2019) 1900699.
[16] H.J. Song, M.C. Sung, H. Yoon, et al., Adv. Sci. 6 (2019) 1802135.
[17] D.S. Baek, G.Y. Jung, B. Seo, et al., Adv. Funct. Mater. 29 (2019) 1901217.
[18] K. Xia, J. Guo, C. Xuan, et al., Chin. Chem. Lett. 30 (2019) 192–196.
[19] J. Yu, W. Yu, B. Chang, et al., Chin. Chem. Lett. 33 (2022) 3231–3235.
[20] Y. Ren, H. Wang, T. Zhang, et al., Chin. Chem. Lett. 32 (2021) 2243–2248.
[21] J. Sun, L. Guo, M. Gao, et al., Chin. Chem. Lett. 31 (2020) 1670–1673.
[22] D.S. Baek, J. Lee, J. Kim, et al., ACS Catal. 12 (2022) 7415–7426.
[23] W. Wang, Y. Wu, Y. Lin, et al., Adv. Funct. Mater. 32 (2022) 2108464.
[24] X. Fan, C. Liu, M. Wu, et al., Appl. Catal. B: Environ. 318 (2022) 121867.
[25] K.T. Jung, W.B. Kim, C.H. Rhee, et al., Chem. Mater. 16 (2004) 307–314.
[26] X. Sun, J. Yu, X. Tong, et al., J. Energy Chem. 62 (2021) 191–197.
[27] X. Sun, J. Yu, S. Cao, et al., J. Am. Chem. Soc. 144 (2022) 22589–22598.
[28] X. Zhang, T. Liu, T. Guo, et al., ACS Appl. Mater. Interfaces 13 (2021) 40705–40712.
[29] M. Hu, H. Chen, B. Liu, et al., Appl. Catal. B: Environ. 317 (2022) 121774.
[30] P. Chen, L. Ouyang, C. Lang, et al., ACS Sustain. Chem. Eng. 11 (2023) 3585–3593.
[31] Y. Zhang, D. Kong, L. Bo, et al., ACS Appl. Energy Mater. 4 (2021) 13051–13060.
[32] S.T. Oyama, Catal. Today 15 (1992) 179–200.
[33] P. Yin, H. Cai, X. Zhang, et al., New J. Chem. 45 (2021) 10396–10401.
[34] Y. Ma, M. Chen, H. Geng, et al., Adv. Funct. Mater. 30 (2020) 2000561.
[35] X. Zhou, Y. Tian, J. Luo, et al., Adv. Funct. Mater. 32 (2022) 2201518.
[36] Y. Kanai, K. Terasaka, S. Fujioka, et al., J. Chem. Eng. Jpn. 52 (2019) 31–40.
[37] B. Deng, J. Tang, X. Mao, et al., Environ. Sci. Technol. 50 (2016) 10588–10595.
[38] R. Yu, J. Xiang, K. Du, et al., Nano Lett. 22 (2022) 97–104.
[39] A. Yu, G. Ma, L. Zhu, et al., Appl. Catal. B: Environ. 307 (2022) 121161.
[40] X. Liu, X. Wang, G. Licht, et al., J. CO2 Util. 36 (2020) 288–294.
[41] X. Liu, J. Ren, G. Licht, et al., Adv. Sustain. Syst. 3 (2019) 1900056.
[42] J. Ren, F.F. Li, J. Lau, et al., Nano Lett. 15 (2015) 6142–6148.
[43] A. Yu, G. Ma, J. Ren, et al., ChemSusChem 13 (2020) 6229–6245.
[44] J. Ren, A. Yu, P. Peng, et al., Acc. Chem. Res. 52 (2019) 3177–3187.
[45] W. Liu, X. Wang, J. Qu, et al., Appl. Catal. B: Environ. 307 (2022) 121201.
[46] H. Xiao, H. Zhu, W. Weng, et al., Mater. Chem. Front. 5 (2021) 4963–4969.
[47] W. Liu, X. Wang, F. Wang, et al., Nat. Commun. 12 (2021) 6776.
[48] Y. Chen, B. Gao, M. Wang, et al., Nano Energy 90 (2021) 106533.
[49] J. Shi, L. Hu, J. Liu, et al., J. Mater. Chem. A 10 (2022) 11414–11425.
[50] H.Q. Chang, G.H. Zhang, K.C. Chou, Nanotechnology 33 (2022) 105402.
[51] Q. Lin, C. Shang, Z. Chen, et al., Int. J. Hydrog. Energy 45 (2020) 30659–30665.
[52] S. Yuan, Y. Liu, J. Zheng, et al., J. Alloy. Compd. 933 (2023) 167664.
[53] H.L. Jia, H.C. Li, J. Zhao, et al., New J. Chem. 46 (2022) 15804–15810.
[54] J. Liu, B. Gao, W. Qin, et al., ACS Appl. Energy Mater. 5 (2022) 10482–10489.
[55] J.C. Ruiz-Cornejo, D. Sebastián, J.I. Pardo, et al., J. Power Sources 546 (2022) 231988.
[56] Z. Chen, B. Deng, K. Du, et al., Adv. Sustain. Syst. 1 (2017) 1700047.
[57] J. Wang, F. Xu, H. Jin, et al., Adv. Mater. 29 (2017) 1605838.
[58] C. Li, Z. Wang, M. Liu, et al., Nat. Commun. 13 (2022) 3338.